

Pressure-induced superconductivity and phase transition in PbSe and PbTe

Yuyang Jiang(江宇阳), Cuiying Pei(裴翠颖), Qi Wang(王琦), Juefei Wu(吴珏霏), Lili Zhang(张丽丽), Chao Xiong(熊超), and Yanpeng Qi(齐彦鹏)
Citation: Chin. Phys. B, 2024, 33 (**12**): 126105. DOI: 10.1088/1674-1056/ad8ecc
Journal homepage: http://cpb.iphy.ac.cn; http://iopscience.iop.org/cpb

What follows is a list of articles you may be interested in

Pressure-induced structural, electronic, and superconducting phase transitions in $TaSe_3$

Yuhang Li(李宇航), Pei Zhou(周佩), Chi Ding(丁驰), Qing Lu(鲁清), Xiaomeng Wang(王晓梦), and Jian Sun(孙建)
Chin. Phys. B, 2024, 33 (**10**): 106102. DOI: 10.1088/1674-1056/ad6f92

First-principles study of structural and electronic properties of multiferroic oxide Mn_3TeO_6 under high pressure

Xiao-Long Pan(潘小龙), Hao Wang(王豪), Lei Liu(柳雷), Xiang-Rong Chen(陈向荣), and Hua-Yun Geng(耿华运)
Chin. Phys. B, 2024, 33 (**7**): 076102. DOI: 10.1088/1674-1056/ad3ef6

Ultrafast dynamics in photo-excited Mott insulator $Sr_3Ir_2O_7$ at high pressure

Xia Yin(尹霞), Jianbo Zhang(张建波), Wang Dong(王东), Takeshi Nakagawa, Chunsheng Xia(夏春生), Caoshun Zhang(张曹顺), Weicheng Guo(郭伟程), Jun Chang(昌峻), and Yang Ding(丁阳)
Chin. Phys. B, 2024, 33 (**1**): 016103. DOI: 10.1088/1674-1056/acdc8c

Structural stability and ion migration of Li_2MnO_3 cathode material under high pressures

Ze-Ren Xie(谢泽仁), Si-Si Zhou(周思思), Bei-Bei He(贺贝贝), Huan-Wen Wang(王欢文), Yan-Sheng Gong(公衍生), Jun Jin(金俊), Xiang-Gong Zhang(张祥功), and Rui Wang(汪锐)
Chin. Phys. B, 2023, 32 (**12**): 126101. DOI: 10.1088/1674-1056/ace2b1

Prediction of superionic state in LiH_2 at conditions enroute to nuclear fusion

Fude Li(李福德), Hao Wang(王豪), Jinlong Li(李津龙), and Huayun Geng(耿华运)
Chin. Phys. B, 2023, 32 (**10**): 106103. DOI: 10.1088/1674-1056/acea68

SPECIAL TOPIC — Structures and properties of materials under high pressure

Pressure-induced superconductivity and phase transition in PbSe and PbTe

Yuyang Jiang(江宇阳)[1,†], Cuiying Pei(裴翠颖)[1,†], Qi Wang(王琦)[1,2], Juefei Wu(吴珏霏)[1], Lili Zhang(张丽丽)[3], Chao Xiong(熊超)[1], and Yanpeng Qi(齐彦鹏)[1,2,4,‡]

[1] *School of Physical Science and Technology, ShanghaiTech University, Shanghai* 201210, *China*
[2] *ShanghaiTech Laboratory for Topological Physics, ShanghaiTech University, Shanghai* 201210, *China*
[3] *Shanghai Synchrotron Radiation Facility, Shanghai Advanced Research Institute, Chinese Academy of Sciences, Shanghai* 201203, *China*
[4] *Shanghai Key Laboratory of High-resolution Electron Microscopy, ShanghaiTech University, Shanghai* 201210, *China*

(Received 29 September 2024; revised manuscript received 1 November 2024; accepted manuscript online 5 November 2024)

The IV–VI semiconducting chalcogenides are a large material family with distinct physical behavior. Here, we systematically investigate the effect of pressure on the electronic and crystal structures of PbSe and PbTe by combining high-pressure electrical transport and synchrotron x-ray diffraction (XRD) measurements. The resistivity of PbSe and PbTe changes dramatically under high pressure and a non-monotonic evolution of $\rho(T)$ is observed. Both PbSe and PbTe are found to undergo semiconductor–metal transition upon compression and show superconductivity under higher pressure. The structural evolutions from the $Fm\bar{3}m$ to *Pnma* phase and then to the $Pm\bar{3}m$ phase in PbSe are verified by the x-ray diffraction. The present findings reveal the internal correlation between the structural evolution and the physical properties in lead chalcogenides.

Keywords: IV–VI semiconductor, high pressure, superconductivity, crystal structure

PACS: 61.50.Ks, 74.70.–b, 74.62.Fj **DOI:** 10.1088/1674-1056/ad8ecc

1. Introduction

The IV–VI semiconductors MX (M = Ge, Sn, Pb; X = S, Se, Te) have been extensively investigated for many years because of their various physical properties and technological applications.[1–3] Among them, PbX materials were well known for high carrier mobility as well as high ZT value in mid-temperature region thus gained wide applications in solar cells and thermoelectric field.[4,5] Germanium chalcogenides, like GeSe and GeTe, known as phase-change materials, have been used as data storage devices.[6,7] From structure point of view, the IV–VI semiconductors crystallize in three different structures under ambient conditions.[8] The GeS type structure analogous to black phosphorus is observed for the lighter compounds GeS, GeSe, SnS and SnSe. Compounds SnTe, PbS, PbSe and PbTe crystallize with the cubic NaCl structure, and GeTe shows a rhombohedral structure as a binary analogue of the gray arsenic.

Pressure, serving as a key thermodynamic parameter, offers a potent means to manipulate crystal and electronic band structures without introducing impurities or defects, thereby unveiling novel physical phenomena that are not observable under ambient conditions.[9–16] As one of the most significant features of the IV–VI compounds, complex structural transitions are observed upon compression.[7,17–25] Initial GeS-type compounds, like SnS and SnSe, undergo two pressure-induced structural transitions: the first from orthorhombic GeS-type structure (space group *Pnma*) to orthorhombic structure (space group *Cmcm*) and then to cubic CsCl-type structure (space group $Pm\bar{3}m$).[19,26,27] PbX (X = Se, Te) and other NaCl-type IV–VI compounds experience a similar evolution path: first from the rocksalt NaCl structure (space group $Fm\bar{3}m$) to a lower symmetrical phase (space group *Pnma*) and then to body-centered cubic CsCl structure (space group $Pm\bar{3}m$).[8,28] Specially, it has been theoretically predicted by Barone *et al.* that external pressure can induce topological phase transitions in PbSe and PbTe within a rocksalt structure.[29]

Another typical phenomenon for the IV–VI compounds under high pressure is the semiconductor–metal transition presented along with the phase transformation.[9,17,18,26,27,30] As pressure increases, a huge reduction of the resistivity emerges and compounds finally enter metallic state. The exact structural evolution with pressure for the IV–VI compounds has been clarified, however, the origin of anomaly in resistivity curve still remains unknown. With many of these compounds, superconductivity was only reported in the 1970s and 1980s,[31–33] it is important to examine the relationship between their electronic transition as well as superconducting properties and the structural transformation under high pressure. Motivated by the above issues, we systematically investigated the effect of pressure on the IV–VI compounds. We chose PbX (X = Se, Te) and studied the evolution of their physical properties and crystal structure under pressure. Com-

[†]These authors contributed equally to this work.
[‡]Corresponding author. E-mail: qiyp@shanghaitech.edu.cn
© 2024 Chinese Physical Society and IOP Publishing Ltd

bining high-pressure electrical transport and synchrotron x-ray diffraction (XRD) measurements, we have drawn a phase diagram for PbSe and PbTe to reveal the internal correlation between the structural evolution and the electrical properties.

2. Methods

Single crystals of PbSe were grown using a chemical vapor transport (CVT) method. High-purity Pb sheets (99.99%) and Se powder (99.99%) were mixed in the proportion of Pb:Se = 1:1 before loaded into a quartz ampoule. The chemical-loaded ampoule was gradually evacuated to vacuum of 10^{-5} torr and sealed. The sealed ampoule was laid in a two-zone horizontal furnace. The source zone and growth zone were heated to 1313 K and 1240 K, respectively, at a rate of 30 K/h. Then temperatures were kept for 5 h and slowly cooled down by 100 K in 10 h. At the completion of the run, the furnace was slowly cooled down to room temperature at a rate of 10 K/h. The as-synthesized single crystals were carefully collected after physical breaking of the ampule.

Single crystals of PbTe were synthesized by mixing stoichiometric ratio of Pb sheets (99.99%) and Te powder (99.99%). The mixture was loaded into an alumina crucible and then stored in a quartz tube. Then the vacuum ampoule was slowly heated to 723 K in 12 h and heated to 1323 K in 7 h and kept for 6 h. Then the tube was steadily cooled to 1123 K in 6 h and subsequently air quenched to room temperature.

Powder x-ray diffraction (XRD) was examined on a Bruker D2 powder x-ray diffractometer (Cu K_α radiation, $\lambda = 1.54056$ Å). Rietveld refinements of the powder XRD patterns were performed through the software of General Structure Analysis System (GSAS-II).[34] Scanning electron microscope (Phenom Pro) equipped with energy dispersive spectroscopy (EDS) was utilized to characterize the composition and detect the surface morphology of the single crystals. Electrical resistivity at ambient pressure was measured using a physical property measurement system (PPMS). We adopted a standard DC four-probe method with Au wires to obtain the electrical resistivity in a temperature range from 1.8 K to 300 K.

A BeCu-type diamond anvil cell (DAC) with 200 μm culet was used to generate high pressure for transport measurements as described elsewhere.[35,36] A layer of cubic BN/epoxy composite was interposed between the BeCu gasket and the electrical contacts. Four pieces of Pt foils were positioned on the sample's surface in accordance with the van der Pauw technique.[10,37,38] The high-pressure XRD experiments were conducted at the BL15U1 beamline of the Shanghai Synchrotron Radiation Facility, utilizing an x-ray wavelength of $\lambda = 0.6199$ Å. A piece of Re was used as the gasket and mineral oil was used as the pressure transmitting medium. The pressure was measured through the ruby luminescence method.[39] Rietveld refinements were applied with the GSAS-II to obtain the structural parameters.[34]

3. Results

As shown in the insets of Figs. 1(a) and 1(b), both PbSe and PbTe samples show metallic luster. The synthesized PbSe and PbTe samples are characterized by the XRD and EDS measurements at ambient pressure. Figures 1(a) and 1(b) show the XRD patterns and Rietveld refinement results for PbSe and PbTe. All the peaks could be attributed to NaCl-type face-centered cubic (fcc) structure with space group of $Fm\bar{3}m$. From the EDS data in Figs. 1(c) and 1(b), the chemical composition Pb:Se = 47.99:52.01 implies slight Pb vacancies in the as-grown samples, while Pb:Te = 53.94:46.06 with slight Te defects.

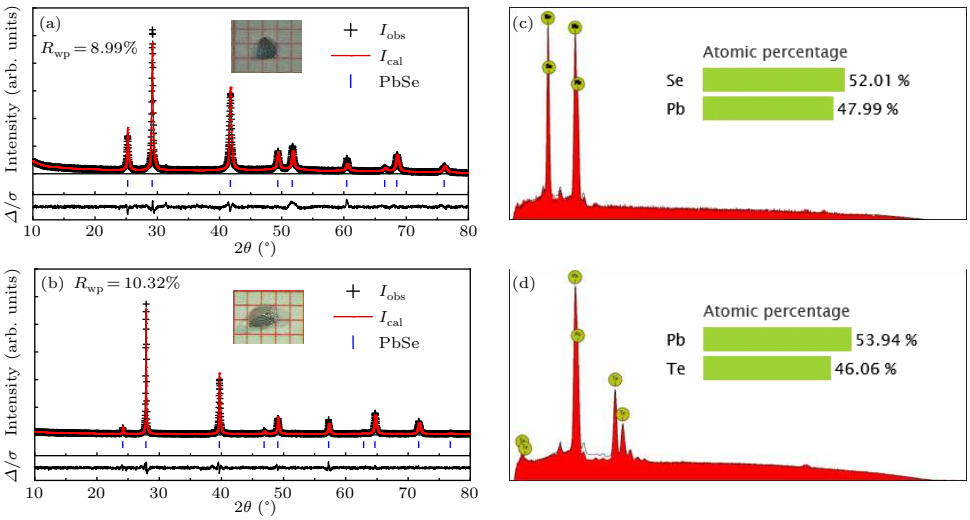


Fig. 1. Powder XRD patterns of (a) PbSe and (b) PbTe. The red solid lines represent the Rietveld fits for the corresponding materials, the black cross symbols correspond to the observed data, the blue perpendicular lines indicate the peak positions and the solid lines at the bottom indicate the residual intensities. The insets show photos of the PbSe and PbTe single crystals. (c) and (d) The energy dispersive x-ray spectra and atomic concentration percentage charts for PbSe and PbTe, respectively.

Figure 2 displays the temperature dependence of the electrical resistivity $\rho(T)$ of PbSe and PbTe ranging from 1.8 K to 300 K. Although electronic structure calculations indicate that both PbSe and PbTe compounds are narrow-gap semiconductors, the $\rho(T)$ for both PbSe and PbTe reveal a metallic behavior in the normal state. We attribute such behavior to the self-doping due to deviations from stoichiometry, causing the variation of Fermi level to metal states. The insets of Fig. 2 show the resistivity in the low temperature region. The residual resistivity ratio [$RRR = \rho(300\ \mathrm{K})/\rho(1.8\ \mathrm{K})$] is 26.8 for PbSe and 60.3 for PbTe.

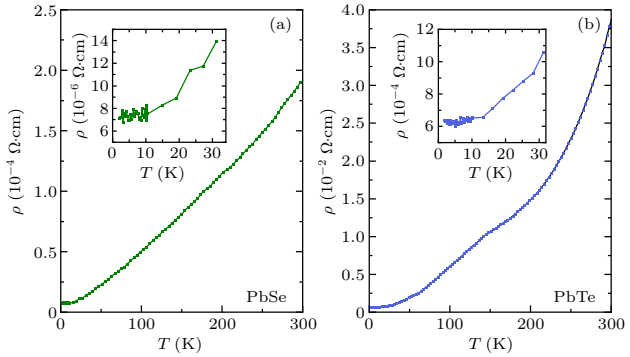


Fig. 2. Resistivity of (a) PbSe and (b) PbTe in zero field from 1.8 K to 300 K. The insets show enlarged pictures of $\rho(T)$ from 1.8 K to 30 K.

Figure 3 shows the temperature dependence of the resistivity $\rho(T)$ of PbSe under various pressures. In the low-pressure region, $\rho(T)$ shows a metallic character similar to that observed at ambient pressure. Increasing pressure initially induces a continuous suppression of the overall magnitude of ρ. Subsequently, $\rho(T)$ decreases rapidly with a minimum occurring at around 2.3 GPa and then increases abnormally. For $P > 3.5$ GPa, $\rho(T)$ displays a semiconducting-like behavior, which is different from that observed in the low-pressure region. These unusual phenomena could be related to a pressure-induced topological phase transition manifested as the band-gap closure and following reopening.[40] Upon further compression, the resistivity reaches a maximum at a pressure above 7 GPa. At the same time, the curve displays a pronounced anomalous peak near 250 K, indicating the metal–insulator transition ($T_{\mathrm{M-I}}$). As the pressure is further increased above 7 GPa, ρ rapidly decreases. At 15.3 GPa, the normal state behaves as a metal. When the pressure increases to around 19.6 GPa, a small drop of ρ is observed below 6.5 K. When the pressure rises up to 23.7 GPa, the resistivity drop becomes more evident and zero resistivity is achieved at low temperature, indicating the emergence of superconductivity in PbSe under pressure.[33] Higher pressure suppresses the superconductivity as the T_{c} decreases. As shown in Fig. 3(e), the high-pressure experiments have been repeated on different samples with good reproducibility of the observed superconductivity transition temperatures. The occurrence of pressure-induced metallization and the following superconducting transition in PbSe are consistent with other MX semiconductors.[27,41–43]

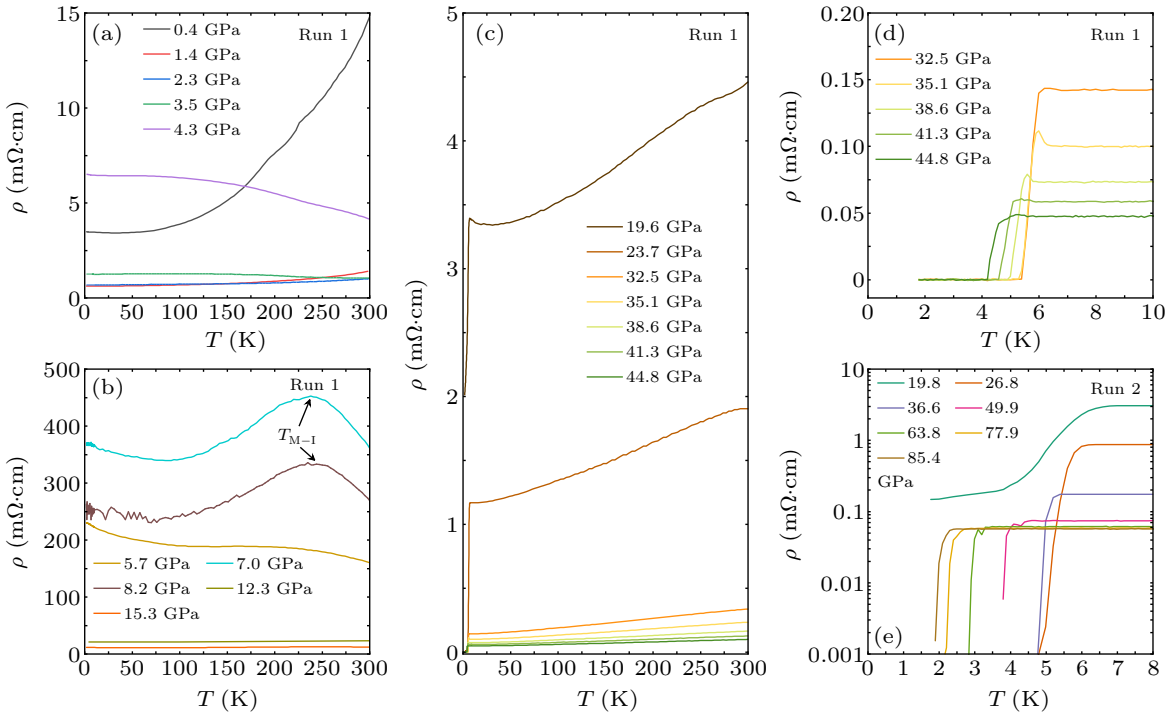


Fig. 3. Characterization of the electrical transport property of PbSe at various pressures. Temperature dependence of resistivity from (a) 0.4–4.3 GPa, (b) 5.7–15.3 GPa and (c) 19.6–44.8 GPa. The superconducting transition and zero-resistivity behavior become clear above 19.6 GPa. (d) Temperature dependence of the resistivity measured in the pressure range from 32.5 GPa to 44.8 GPa around T_{c}. (e) Temperature dependence of the resistivity from 19.8 GPa to 85.4 GPa in run 2 around T_{c}.

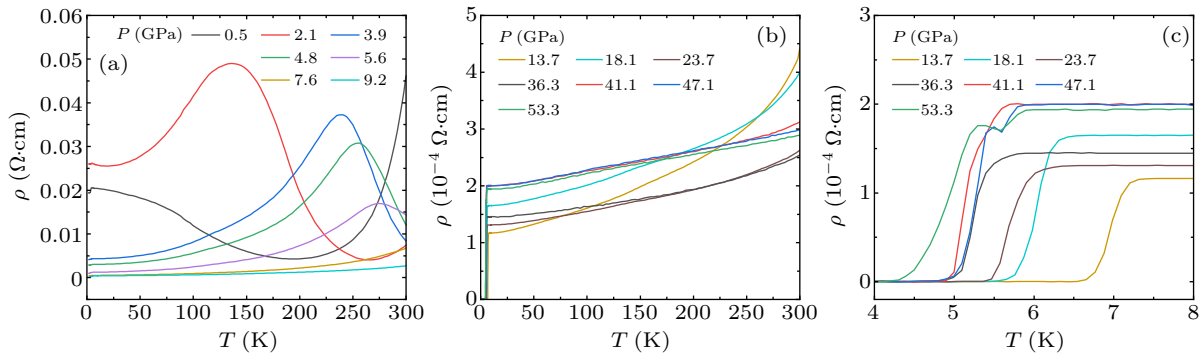


Fig. 4. Characterization of the electrical transport property of PbTe at various pressures. Temperature dependence of resistivity in the pressure ranges of (a) 0.5–9.2 GPa and (b) 13.7–53.3 GPa. The superconducting transition and zero-resistivity can be observed. (c) Temperature dependence of the resistivity measured at different pressures between 13.7 GPa and 53.3 GPa near T_c.

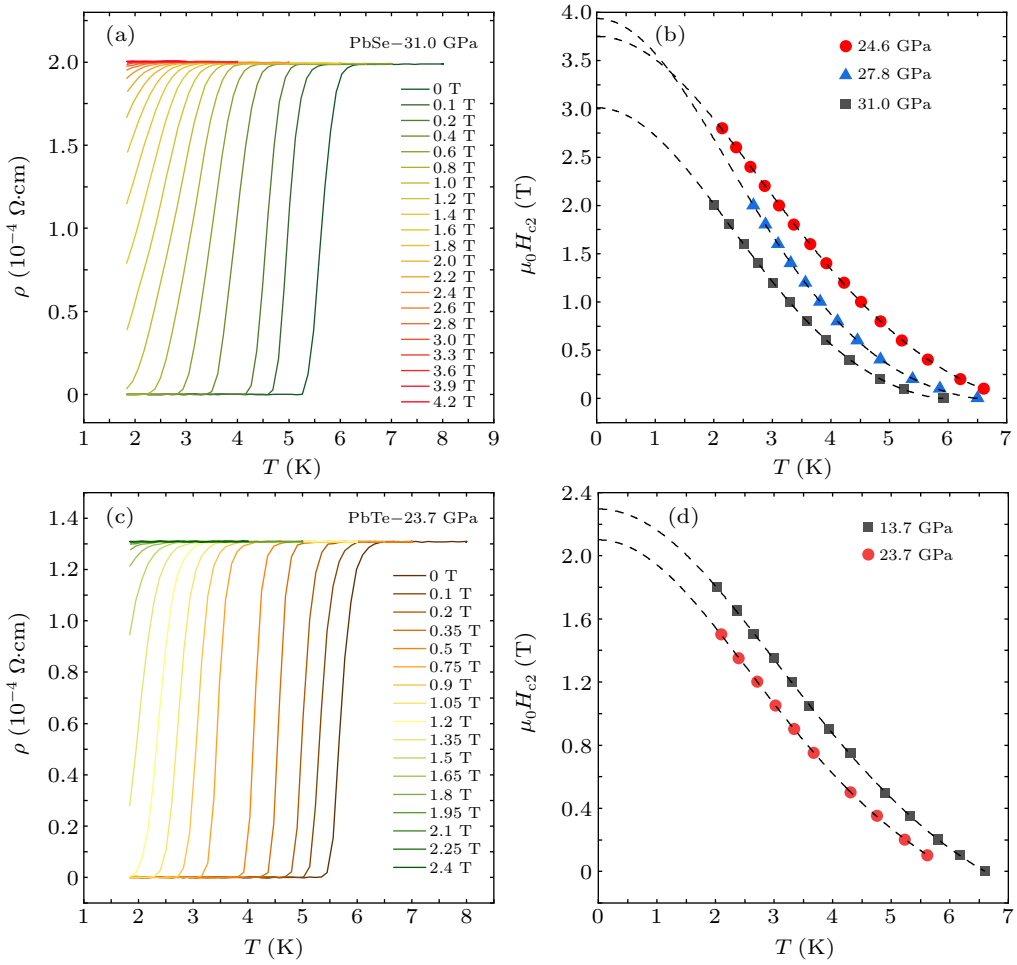


Fig. 5. (a) Electrical resistivity in different magnetic fields for PbSe at 31.0 GPa. (b) The upper critical field $\mu_0 H_{c2}$ as a function of temperature at 24.6 GPa, 27.8 GPa and 31.0 GPa for PbSe, respectively. (c) Electrical resistivity in different magnetic fields for PbTe at 23.7 GPa. (d) The upper critical field $\mu_0 H_{c2}$ as a function of temperature at 13.7 GPa and 23.7 GPa for PbTe, respectively.

We also performed the electrical resistivity measurements of PbTe at various pressures from 1.8 K to 300 K. When the pressure is around 7.6 GPa, $\rho(T)$ shows a metallic behavior as that at ambient pressure. The superconducting transition $T_c^{\text{onset}} \sim 7.2$ K is observed at 13.7 GPa and then decreases with pressure, revealing a negative pressure coefficient of T_c. In summary, a similar evolution of $\rho(T)$ is observed for PbTe under high pressure, and this abnormal phenomenon is closely related to the structural phase transitions which will be discussed hereafter.

The observed superconductivity in PbSe is further supported by the evolution of the resistivity–temperature curve with the magnetic fields applied as shown in Fig. 5(a). The superconductivity is suppressed with increasing magnetic fields. A magnetic field of about 4 T is adequate to suppress the superconducting transition under this pressure. The upper critical field $\mu_0 H_{c2}(T)$ is determined by $\rho = 90\%\rho_0$ (ρ_0 is the initial resistivity before superconducting transition) on the

resistivity–temperature curves, as shown in Fig. 5(b). Deviating from the Werthamer–Helfand–Hohenberg theory based on the single-band model,[44] the upper critical field $\mu_0 H_{c2}(T)$ of PbSe has a positive curvature. Similar behavior has been observed in MgB_2, YNi_2B_2C, 2H-$NbSe_2$ and isostructural superconductor PbS[41,45–49] but neither observed in Cr-doped PbSe nor In–I co-doped PbTe investigated before.[50,51] More detailed study is still required to confirm the multiband superconducting properties in PbSe under high pressure. A simple formula $\mu_0 H_{c2}(T) = \mu_0 H_{c2}(0)[1-(T/T_c)^2]^{\alpha}/[1+(T/T_c)^2]^{\beta}$ is used to fit the $\mu_0 H_{c2}(T)$ curves.[52] We obtain $\alpha = 1.50$ and $\beta = 2.02$ for PbSe at 31.0 GPa, which is far from the value of 1 in the Ginzburg–Landau model.[53,54] The zero-temperature upper critical field is estimated to be 3.01 T at 31.0 GPa, which yields a coherence length $\xi(0)$ of 10.3 nm according to the Ginzburg–Landau equation.[55] It is worth noting that the value of $\mu_0 H_{c2}(0)$ is well below the Pauli–Clogston limit. Similarly, the estimated $\mu_0 H_{c2}(0)$ is 3.65 T and 3.93 T at 24.6 GPa and 27.8 GPa, respectively. Figure 5(c) shows the evolution of the superconductivity of PbTe in the magnetic field at 23.7 GPa. The superconducting transition is gradually suppressed as the magnetic field increases to 2.4 T, with the extrapolated upper critical field $\mu_0 H_{c2}(0)$ to be 2.1 T (2.29 T) at 23.7 GPa (13.7 GPa), as shown in Fig. 5(d). The response of temperature dependence of the resistivity to magnetic fields in both PbSe and PbTe provides further evidence of the pressure-induced superconducting transition.

To identify the origin of the superconducting transition and the anomaly in the resistivity curve, we chose PbSe to perform *in situ* high-pressure XRD measurements to analyze the structural evolution under various pressures. Figure 6(a) shows the high-pressure synchrotron XRD patterns measured at room temperature up to 72.6 GPa. As shown in the patterns below 4.6 GPa, we can index all the diffraction peaks of PbSe with the $Fm\bar{3}m$ phase. Beyond 5.9 GPa, we observe a structural transformation in particularly characterized by the emergence of a new diffraction peak near $2\theta = 12.5°$. The signal of $Fm\bar{3}m$ phase completely eliminates at around 9.0 GPa, which is consistent with the rapid decrease of resistivity in our electrical transport measurements in Fig. 3. Above 21.4 GPa, another phase transition takes place, as indicated by the new diffraction peaks in the XRD patterns in Fig. 6(a). Upon compression to 35.8 GPa, the XRD patterns remain the same shape and no further transitions are observed within 72.6 GPa. All the peaks can correspond to the phase with space group $Pm\bar{3}m$.

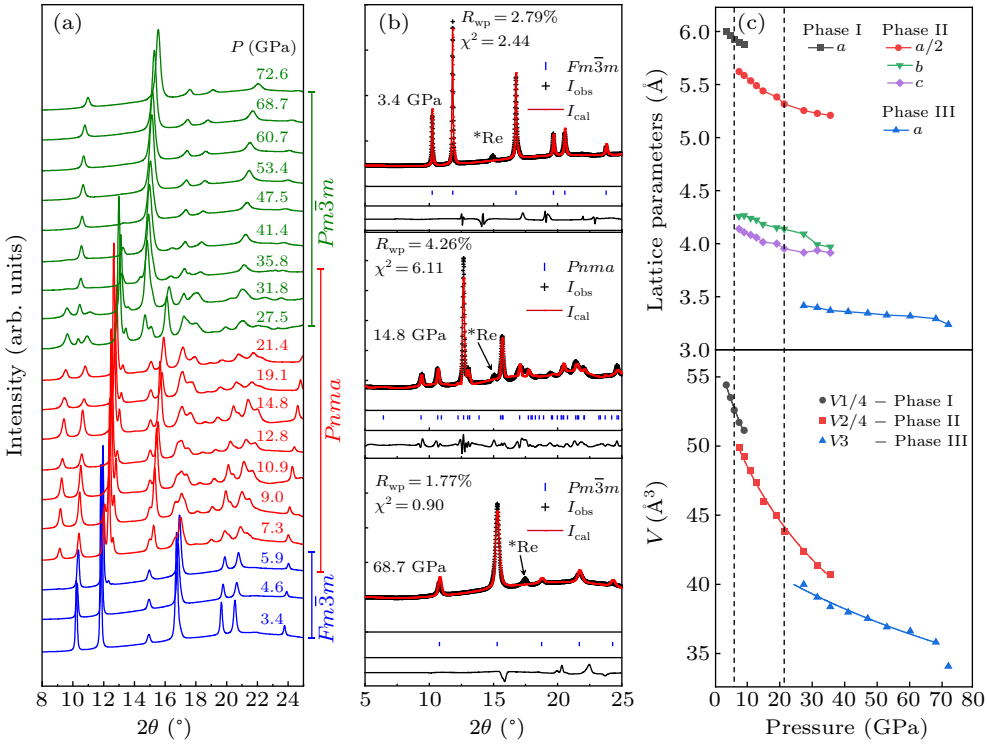


Fig. 6. (a) High-pressure XRD patterns of PbSe at room temperature up to 72.6 GPa. (b) The representative XRD patterns of PbSe at 3.4 GPa, 14.8 GPa and 68.7 GPa, respectively. The red solid lines represent the Rietveld fits for the corresponding materials, the black cross symbols correspond to the observed data, the blue perpendicular lines indicate the peak positions and the solid lines at the bottom indicate the residual intensities. (c) Pressure dependence of lattice parameters and the unit-cell volume of PbSe for $Fm\bar{3}m$, *Pnma* and $Pm\bar{3}m$ phases, respectively.

The representative fittings of the XRD patterns obtained at 3.4 GPa, 14.8 GPa, and 68.7 GPa are displayed in Fig. 6(b). Three phases with the space groups of $Fm\bar{3}m$, *Pnma* and $Pm\bar{3}m$ are demonstrated by the reasonable refinements. The refinements yield model parameters of $R_{wp} = 2.79\%$ and $\chi^2 = 2.44$ for the $Fm\bar{3}m$ phase, $R_{wp} = 4.26\%$ and $\chi^2 = 6.11$ for the *Pnma* phase and $R_{wp} = 1.77\%$ and $\chi^2 = 0.90$ for the $Pm\bar{3}m$ phase. The corresponding fitting results are summarized in

Table 1. Among the three phases, the *Pnma* structure can be created by an orthorhombic distortion from the $Fm\bar{3}m$ structure, and the atoms slide in *Pnma* could lead to the structure transition to $Pm\bar{3}m$ under higher pressure.[28,56]

Table 1. Structural parameters of PbSe under high pressure.

Phase	I	II	III
Pressure (GPa)	3.4	14.8	68.7
Crystal system	cubic	orthorhombic	cubic
Space group	$Fm\bar{3}m$	*Pnma*	$Pm\bar{3}m$
Z	4	1	4
a, b, c (Å)	$a, b, c = 6.0162(1)$	$a = 10.9116(2)$	$a, b, c = 3.2934(2)$
α, β, γ (°)	$\alpha = \beta = \gamma = 90.00000$	$b = 4.1911(7)$	$\alpha = \beta = \gamma = 90.00000$
		$c = 4.0210(6)$	
		$\alpha = \beta = \gamma = 90.00000$	
Cell volume (Å^3)	217.76(1)	183.89(3)	35.723(8)
Density (g·cm^{-3})	8.679	8.430	11.827
R_{wp} (%)	2.79	4.26	1.77
χ^2	2.44	6.11	0.90

Figure 6(c) presents the pressure-dependent lattice parameters and volume of the three phases in PbSe. There are two coexistence regions around the phase transition pressures. The $Fm\bar{3}m$ phase coexists with *Pnma* phase between 5.9 GPa and 7.3 GPa, and *Pnma* phase is along with $Pm\bar{3}m$ phase between 27.5 GPa and 35.8 GPa. It should be noted that the *Pnma* phase has a doubled lattice period compared with the $Fm\bar{3}m$ phase. This phenomenon indicates that the phase transition from $Fm\bar{3}m$ to *Pnma* is mediated by a Peierls distortion.[28,56] The phase III is more symmetric in comparison with phase II, which suggests that phase III is derived by the pressure-suppressed Peierls distortion. In Fig. 6(b), we use a third-order Birch–Murnaghan equation of state to fit the volume–pressure relation. The equation is

$$P = \frac{3B_0}{2}\left[\left(\frac{V_0}{V}\right)^{7/3} - \left(\frac{V_0}{V}\right)^{5/3}\right] \times \left\{1 + \frac{3}{4}(B_0' - 4)\left[\left(\frac{V_0}{V}\right)^{2/3} - 1\right]\right\}, \quad (1)$$

where B_0 and V_0 are the bulk modulus and unit-cell volume, respectively. The fitting yields $B_0 = 63.40 \pm 5.13$ GPa and $V_0 = 57.07 \pm 0.33$ Å^3 for the $Fm\bar{3}m$ phase, $B_0 = 64.77 \pm 3.4$ GPa and $V_0 = 54.72 \pm 0.44$ Å^3 for the *Pnma* phase and $B_0 = 227.36 \pm 22.72$ GPa and $V_0 = 43.68 \pm 0.52$ Å^3 for the $Pm\bar{3}m$ phase. We use the volume per unit cell ($Z = 4$ for the $Fm\bar{3}m$ and $Pm\bar{3}m$ phases and $Z = 1$ for the *Pnma* phase) to elucidate the volume evolution of the three phases upon compression. The volume collapses from the $Fm\bar{3}m$ to *Pnma* phase and from the *Pnma* to $Pm\bar{3}m$ phase are 3.5% and 5.7%, respectively, providing the evidence of the first-order transition.

Figure 7(a) shows the high-pressure phase diagram of PbSe encompassing the T_c, resistivity at typical temperatures and temperature coefficient of the resistivity ($d\rho/dT$) acquired from transport measurements. These results demonstrate that high pressure dramatically alters both crystal and electronic structures of PbSe. Upon compression, PbSe experiences the similar evolution path as other IV–VI compounds: first from $Fm\bar{3}m$ structure to *Pnma* structure, and then to $Pm\bar{3}m$ structure. The resistivity of PbSe exhibits a nonmonotonic evolution with increasing pressure, which corresponds to a semiconductor–metal transition. In phase I, the resistivity is first suppressed with applied pressure and reaches a relatively low value at about 2.3 GPa. This peculiar behavior of resistivity is not associated with a structural phase transition because high-pressure XRD studies reveal structural stability in this pressure range. The emergence of the sharp valley has been identified as a signature of pressure-induced topological phase transition. A similar phenomenon was observed for black phosphorus,[57] Sb_2Te_3,[58] $ZrTe_2$,[59] BiTeI,[60] and $TlBiS_2$.[11] As the pressure further increases, the resistivity increases with a maximum occurring at around 7.0 GPa with a temperature-dependent metal–insulator transition, indicating the completion of the first structural transition.

In phase II, the slope of the pressure dependent resistivity has an obvious change. The resistivity begins to decrease upon compression which is obviously different from the behavior in Cr-doped PbSe.[50] In phase III, the resistivity continuously decreases with pressure and exhibits typical metallic behavior. The slope becomes moderate under higher pressure. Superconductivity is observed in this pressure region and the T_c decreases monotonically with increasing pressure. The observed superconductivity in PbSe is associated with structural instability and/or pressure-induced structural phase transition. The suppression of superconductivity in phase III is probably due to a reduction of the density of state at the Fermi level as revealed by a study of PbS.[41]

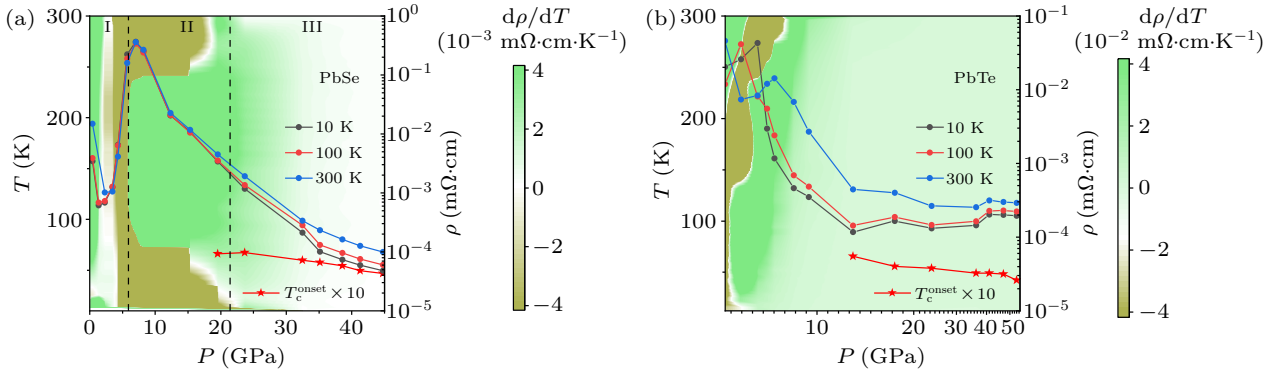


Fig. 7. Phase diagram of (a) PbSe and (b) PbTe. The blue, red and black lines represent the variation in resistivity with temperature at 10 K, 100 K and 300 K, respectively. Dashed lines correspond to onsets of phase transition. Red stars represent superconducting transition temperature T_c. The background represents the dependence of $\mathrm{d}\rho/\mathrm{d}T$ from 1.8 K to 300 K at different pressures.

A quite similar evolution under high pressure is observed in PbTe. All the characteristic temperatures from our high-pressure experiments are summarized in a T–P phase diagram in Fig. 7(b). Pressure-induced non-monotonic evolution of resistivity and a metal–semiconductor transition occur in PbTe at the low-pressure region in accordance with the pressure of structural transition reported before.[23] Upon further compression, PbTe evolves into a metallic state at the normal state, and superconductivity is observed at low temperatures. The results presented above allow us to build the close relationship between the structural and physical properties for PbX material under high pressures. Further investigation combining first principles calculations could be significant to clarify the mechanism of the pressure-induced superconductivity in the IV–VI semiconductors.[41,61]

4. Conclusion

In this work, we conducted a comprehensive characterization of the structural evolution and superconductivity of lead chalcogenides PbSe and PbTe. *In situ* high-pressure synchrotron XRD experiments along with Rietveld refinements confirmed the structural transition from the $Fm\bar{3}m$ to $Pnma$ phase and then to the $Pm\bar{3}m$ phase. High-pressure electrical resistivity measurements demonstrated that both PbSe and PbTe exhibit a quite similar evolution under increasing pressure, from a semiconductor with higher resistivity to a metallic state. Superconductivity emerges when the material evolves into the high-pressure CsCl-type cubic phase. We built a phase diagram for PbSe and PbTe, which can also be extended to other similar IV–VI semiconductors.

Acknowledgments

Project supported by the National Natural Science Foundation of China (Grant No. 52272265) and the National Key R&D Program of China (Grant No. 2023YFA1607400). The authors thank the support from Analytical Instrumentation Center (# SPSTAIC10112914), SPST, ShanghaiTech University. The authors thank the staff members at BL15U1 in Shanghai Synchrotron Radiation Facility for assistance during data collection.

References

[1] Zhou X, Zhang Q, Gan L, Li H, Xiong J and Zhai T 2016 *Adv. Sci.* **3** 1600177
[2] Dobrowolski W, Arciszewska M, Brodowska B, Domukhovski V, Dugaev V, Grzęda A, Kuryliszyn-Kudelska I, Wójcik M and Slynko E 2006 *Sci. Sintering* **38** 109
[3] Xiao G, Wang Y, Ning J, Wei Y, Liu B, William W Y, Zou G and Zou B 2013 *RSC Adv.* **3** 8104
[4] Korkosz R J, Chasapis T C, Lo S H, Doak J W, Kim Y J, Wu C I, Hatzikraniotis E, Hogan T P, Seidman D N and Wolverton C 2014 *J. Am. Chem. Soc.* **136** 3225
[5] Fu H and Tsang S W 2012 *Nanoscale* **4** 2187
[6] Matsunaga T, Akola J, Kohara S, Honma T, Kobayashi K, Ikenaga E, Jones R O, Yamada N, Takata M and Kojima R 2011 *Nat. Mater.* **10** 129
[7] Xu K, Miao X and Xu M 2019 *Phys. Status Solidi Rapid Res. Lett.* **13** 1800506
[8] Chattopadhyay T, Werner A, Von Schnering H and Pannetier J 1984 *Revue de Physique Appliquée* **19** 807
[9] Cheng H, Yao H, Xu Y, Jiang J, Yang Y, Wang J, Li X, Li Y and Shao J 2024 *Chem. Mater.* **36** 3764
[10] Pei C, Zhang J, Wang Q, Zhao Y, Gao L, Gong C, Tian S, Luo R, Li M and Yang W 2023 *Natl. Sci. Rev.* **10** nwad034
[11] Pei C, Huang P, Zhu P, Liu L, Wang Q, Zhao Y, Gao L, Li C, Cao W and Lv J 2022 *Cell Rep. Phys. Sci.* **3** 101094
[12] Sun J, Jiao Y, Yi C, Dissanayake S, Matsuda M, Uwatoko Y, Shi Y, Li Y, Fang Z and Cheng J G 2019 *Phys. Rev. Lett.* **123** 047201
[13] Yu H, Gao D, Wang X, Du X, Lin X, Guo W, Zou R, Jin C, Li K and Chen Y 2018 *NPG Asia Mater.* **10** 882
[14] Zhang L, Wang Y, Lv J and Ma Y 2017 *Nat. Rev. Mater.* **2** 17013
[15] Zhu S, Zhu B, Pei C, Wang Q, Chen J, Zhang Q, Ying T, Gu L, Zhao Y and Li C 2024 *Mater. Today Phys.* **42** 101377
[16] Li T, Wang S, Chen X, Chen C, Fang Y and Yang Z 2024 *Chin. Phys. B* **33** 066401
[17] Dias R P, Kim M and Yoo C S 2016 *Phys. Rev. B.* **93** 104107
[18] Wang S, Zang C, Wang Y, Wang L, Zhang J, Childs C, Ge H, Xu H, Chen H and He D 2015 *Inorg. Chem.* **54** 4981
[19] Ehm L, Knorr K, Dera P, Krimmel A, Bouvier P and Mezouar M 2004 *J. Phys.: Condens. Matter* **16** 3545
[20] Onodera A, Sakamoto I, Fujii Y, Mo N and Sugai S 1997 *Phys. Rev. B* **56** 7935
[21] Zhou D, Li Q, Ma Y, Cui Q and Chen C 2013 *J. Phys. Chem. C* **117** 5352
[22] Li Y, Lin C, Xu J, Li G, Li X and Liu J 2014 *AIP Adv.* **4** 127112

[23] Rousse G, Klotz S, Saitta A, Rodriguez-Carvajal J, McMahon M, Couzinet B and Mezouar M 2005 *Phys. Rev. B* **71** 224116

[24] Pei C, Zhu P, Li B, Zhao Y, Gao L, Li C, Zhu S, Zhang Q, Ying T and Gu L 2023 *Sci. China Mater.* **66** 2822

[25] Ovsyannikov S V, Shchennikov V V, Manakov A Y, Likhacheva A Y, Ponosov Y S, Mogilenskikh V E, Vokhmyanin A P, Ancharov A I and Skipetrov E P 2009 *Phys. Status Solidi (b)* **246** 615

[26] Lv X, Li S, Huang Y and Cui T 2024 *Phys. Rev. B* **110** 054107

[27] Chen X, Lu P, Wang X, Zhou Y, An C, Zhou Y, Xian C, Gao H, Guo Z and Park C 2017 *Phys. Rev. B* **96** 165123

[28] Li Y, Lin C, Li H, Li X and Liu J 2013 *High Pressure Res.* **33** 713

[29] Barone P, Rauch T, Di Sante D, Henk J, Mertig I and Picozzi S 2013 *Phys. Rev. B* **88** 045207

[30] Ravindran R and Asokamani R 1994 *AIP Conf. Proc.* **309** 669

[31] Timofeev Y A, Vinogradov B and Begoulev V 1997 *Phys. Solid State* **39** 207

[32] Timofeev Y A, Vinogradov B, Begoulev V and Yakovlev E N 1986 *Fizika Tverdogo Tela* **28** 2841

[33] Brandt N, Gitsu D, Popovich N, Sidorov V and Chudinov S 1975 *JETP Lett.* **22** 104

[34] Toby B H and Von Dreele R B 2013 *J. Appl. Crystallogr.* **46** 544

[35] Pei C, Ying T, Zhao Y, Gao L, Cao W, Li C, Hosono H and Qi Y 2022 *Matter Radiat. Extremes* **7** 038404

[36] Wang Q, Kong P, Shi W, Pei C, Wen C, Gao L, Zhao Y, Yin Q, Wu Y and Li G 2021 *Adv. Mater.* **33** 2102813

[37] Pei C, Zhang J, Gong C, Wang Q, Gao L, Zhao Y, Tian S, Cao W, Li C and Lu Z Y 2022 *Sci. China Phys., Mech. Astron.* **65** 287412

[38] Zhao Y, Ying T, Zhao L, Wu J, Pei C, Chen J, Deng J, Zhang Q, Gu L and Wang Q 2024 *Adv. Mater.* **36** 2401118

[39] Mao H, Xu J A and Bell P 1986 *J. Geophys. Res.: Solid Earth* **91** 4673

[40] Chen L C, Chen P Q, Li W J, Zhang Q, Struzhkin V V, Goncharov A F, Ren Z and Chen X J 2019 *Nat. Mater.* **18** 1321

[41] Zhang H, Zhong W, Meng Y, Yue B, Yu X, Wang J T and Hong F 2023 *Phys. Rev. B* **107** 174502

[42] Wang Y, Wang K, Ma Y, Zhou M, Wang H and Liu G 2021 *J. Phys.: Condens. Matter* **33** 355403

[43] Matsumoto R, Song P, Adachi S, Saito Y, Hara H, Yamashita A, Nakamura K, Yamamoto S, Tanaka H and Irifune T 2019 *Phys. Rev. B* **99** 184502

[44] Werthamer N, Helfand E and Hohenberg P 1966 *Phys. Rev.* **147** 295

[45] Xu H S, Yan Y J, Yin R, Xia W, Fang S, Chen Z, Li Y, Yang W, Guo Y and Feng D L 2021 *Phys. Rev. Lett.* **127** 187004

[46] Noat Y, Silva-Guillén J A, Cren T, Cherkez V, Brun C, Pons S, Debontridder F, Roditchev D, Sacks W and Cario L 2015 *Phys. Rev. B* **92** 134510

[47] Zocco D, Grube K, Eilers F, Wolf T and Löhneysen H V 2013 *Phys. Rev. Lett.* **111** 057007

[48] Choi H J, Roundy D, Sun H, Cohen M L and Louie S G 2002 *Nature* **418** 758

[49] Kohara T, Oda T, Ueda K, Yamada Y, Mahajan A, Elankumaran K, Hossian Z, Gupta L, Nagarajan R and Vijayaraghavan R 1995 *Phys. Rev. B* **51** 3985

[50] Chen L C, Chen P Q, Li W J, Zhang Q, Struzhkin V V, Goncharov A F, Ren Z and Chen X J 2021 *Phys. Rev. B* **103** 214516

[51] Chen L C, Yu H, Wang X Y, Zhang Q, Struzhkin V V and Chen X J 2022 *Phys. Rev. B* **105** 174503

[52] Wang E, Zhu X and Wen H H 2016 *Europhys. Lett.* **115** 27007

[53] Woollam J A, Somoano R B and O'Connor P 1974 *Phys. Rev. Lett.* **32** 712

[54] Jones C, Hulm J and Chandrasekhar B 1964 *Rev. Mod. Phys.* **36** 74

[55] Talantsev E F 2022 *Rev. Sci. Instrum.* **93** 053912

[56] Wang S, Zhang J, Zhang Y, Alvarado A, Attapattu J, He D, Wang L, Chen C and Zhao Y 2013 *Inorg. Chem.* **52** 8638

[57] Li X, Sun J, Shahi P, Gao M, MacDonald A H, Uwatoko Y, Xiang T, Goodenough J B, Cheng J and Zhou J 2018 *Proc. Natl. Acad. Sci. USA* **115** 9935

[58] Zhang J, Hu T, Yan J, Ke F, Wang J, Cui X, Li X, Ma Y, Yang J and Gao C 2017 *Mater. Lett.* **209** 78

[59] Zhu S, Wu J, Zhu P, Pei C, Wang Q, Jia D, Wang X, Zhao Y, Gao L and Li C 2023 *Adv. Sci.* **10** 2301332

[60] Qi Y, Shi W, Naumov P G, Kumar N, Sankar R, Schnelle W, Shekhar C, Chou F C, Felser C and Yan B 2017 *Adv. Mater.* **29** 1605965

[61] Li Y, Zhou P, Ding C, Lu Q, Wang X and Sun J 2024 *Chin. Phys. B* **33** 106102